Predicting the microvascular invasion and tumor grading of intrahepatic mass-forming cholangiocarcinoma based on magnetic resonance imaging radiomics and morphological features

Shuang Chen[1], Yumeng Zhu[2], Lijuan Wan[1], Shuangmei Zou[3#], Hongmei Zhang[1#]

[1]Department of Diagnostic Radiology, National Cancer Center/National Clinical Research Center for Cancer/Cancer Hospital, Chinese Academy of Medical Sciences and Peking Union Medical College, Beijing, China; [2]Beijing No. 4 High School International Campus, Beijing, China; [3]Department of Pathology, National Cancer Center/National Clinical Research Center for Cancer/Cancer Hospital, Chinese Academy of Medical Sciences and Peking Union Medical College, Beijing, China

Contributions: (I) Conception and design: S Chen, S Zou, H Zhang; (II) Administrative support: H Zhang; (III) Provision of study materials or patients: S Chen, H Zhang; (IV) Collection and assembly of data: S Chen, Y Zhu, L Wan, H Zhang; (V) Data analysis and interpretation: S Chen, Y Zhu; (VI) Manuscript writing: All authors; (VII) Final approval of manuscript: All authors.

[#]These authors contributed equally to this work.

Correspondence to: Hongmei Zhang, PhD. Department of Diagnostic Radiology, National Cancer Center/National Clinical Research Center for Cancer/Cancer Hospital, Chinese Academy of Medical Sciences and Peking Union Medical College, 17 Panjiayuan Nanli, Chaoyang District, Beijing 100021, China. Email: 13581968865@163.com.

Background: Preoperative diagnosis of microvascular invasion (MVI) and tumor grading of intrahepatic mass-forming cholangiocarcinoma (IMCC) using imaging findings can facilitate patient treatment decision-making. This study was conducted to establish and validate nomograms based on magnetic resonance imaging (MRI) radiomics and morphological features for predicting the MVI and tumor grading of IMCC before radical hepatectomy.

Methods: A total of 235 patients with resected IMCC at the Chinese Academy of Medical Sciences and Peking Union Medical College were divided into a training set (n=167) and a validation set (n=68), retrospectively. Clinical data and MRI morphological features were recorded. Univariate and multivariate analyses were conducted to identify the significant features for the prediction of MVI and tumor grading. Radiomics features were extracted from T2-weighted imaging fat-suppressed and diffusion-weighted imaging (DWI). Radiomics signatures (rad_scores) were built based on the least absolute shrinkage and selection operator (LASSO) method. Then, the nomograms were constructed by combining the rad_scores and the significant clinical or MRI morphologic features. The predictive performances for MVI and tumor grading were evaluated by the area under the receiver operating characteristic curve (AUC), calibration, and clinical utility.

Results: Totals of 16 and 9 radiomics features were selected to build the rad_scores for the prediction of MVI and tumor grading for the training and validation set, respectively. The nomogram for the prediction of MVI comprised the morphologic features including number of tumors, tumor margin, and rad_score. For the prediction of tumor grading, the nomogram comprised the number of tumors, tumor necrosis, and rad_ score. The best discriminations were observed in the training and validation sets for the MVI nomogram [AUCs of 0.874, 95% confidence interval (CI): (0.822–0.926) and 0.869 (0.783–0955)] and tumor grading nomogram [AUCs of 0.827 (0.763–0.891) and 0.848 (0.759–0.937)]. Decision curve analysis (DCA) further confirmed the clinical utilities of the nomograms.

Conclusions: Nomograms based on MRI radiomics and morphological features can effectively predict the individualized risks of MVI and tumor grading for IMCC.

Keywords: Biomarkers; intrahepatic mass-forming cholangiocarcinoma (IMCC); magnetic resonance imaging (MRI); radiomics; nomogram

Introduction

The incidence of intrahepatic cholangiocarcinoma (IHC) has risen progressively worldwide (1,2), and the most common morphological subtype is intrahepatic mass-forming cholangiocarcinoma (IMCC) (3,4). Surgical resection is the first-line treatment option; however, even though surgical techniques have greatly improved in recent decades, patients still have a poor outcome, with a 5-year survival rate of approximately 30–35% (5). The poor outcome is mainly related to the high postoperative recurrence rate, with recurrence occurring in approximately 50–70% of cases (6).

Microvascular invasion (MVI) and tumor grading are regarded as 2 of the most important prognostic factors that strongly influence not only tumor recurrence but also patients' survival (7-10). MVI refers to the presence of tumor cells within the within a vascular lumen which is covered by endothelium that is visible only by microscopy (11). MVI is a potential source of intrahepatic metastases and distant metastatic spread, and also is associated with aggressive and progressive tumor behaviors (12). It has been accepted that for patients with a high probability of MVI, large safety margins are needed at surgical resection (13). Considering the strong correlation between tumor grading and lymph node metastases, although it may not be required by all patients, the high tumor grading of IMCC should prompt surgeons to consider portal lymphadenectomy (14). Therefore, the early and precise detection of MVI and tumor grading before treatment is necessary to provide patients with appropriate surgical decisions and prognoses. Generally, biopsy is not a satisfactory method for the diagnosis of MVI or tumor grading preoperatively because of the inadequate tumor specimen obtained and its invasive nature (15).

Medical imaging has provided a noninvasive method for the preoperative assessment of IHC. Specifically, magnetic resonance imaging (MRI) is a common imaging method for IMCC. Some studies have evaluated the correlations between MRI morphological features and MVI for IMCC, and large tumor size and intrahepatic duct dilatation were reported as independent predictors of MVI (16-18). However, the interobserver agreements of MRI morphological features lack further analyses, and the evaluation of these features is highly subjective and variable. Additionally, due to the limitation of the number of patients, those studies lacked sufficient validation. Radiomics can extract high-throughput imaging features from biomedical images and convert them into mineable data for quantitative analysis, with the aim of predicting the pathological characteristics of tumors (19). Recently, MRI-based radiomics nomograms have been found to be helpful in predicting MVI in preliminary studies (18,20). With the increase of the radiomics signatures (rad_scores), the possibility of MVI has increased gradually (18,20). To date, few studies have described the relationship between tumor grading in IMCC and MRI-based radiomics features.

Therefore, this study aimed to develop and validate noninvasive MRI-based radiomics nomograms to predict the biological MVI and tumor grading of IMCC, which are essential for a complete understanding of the stratification of the tumor and to guide more accurate personalized treatment in the future. We present this article in accordance with the TRIPOD reporting checklist (available at https://qims.amegroups.com/article/view/10.21037/qims-23-11/rc).

Methods

The study was conducted in accordance with the Declaration of Helsinki (as revised in 2013). The study was approved by the Ethics Committee of the National Cancer Center/Cancer Hospital, Chinese Academy of Medical Sciences and Peking Union Medical College, and the requirement for individual consent for this retrospective
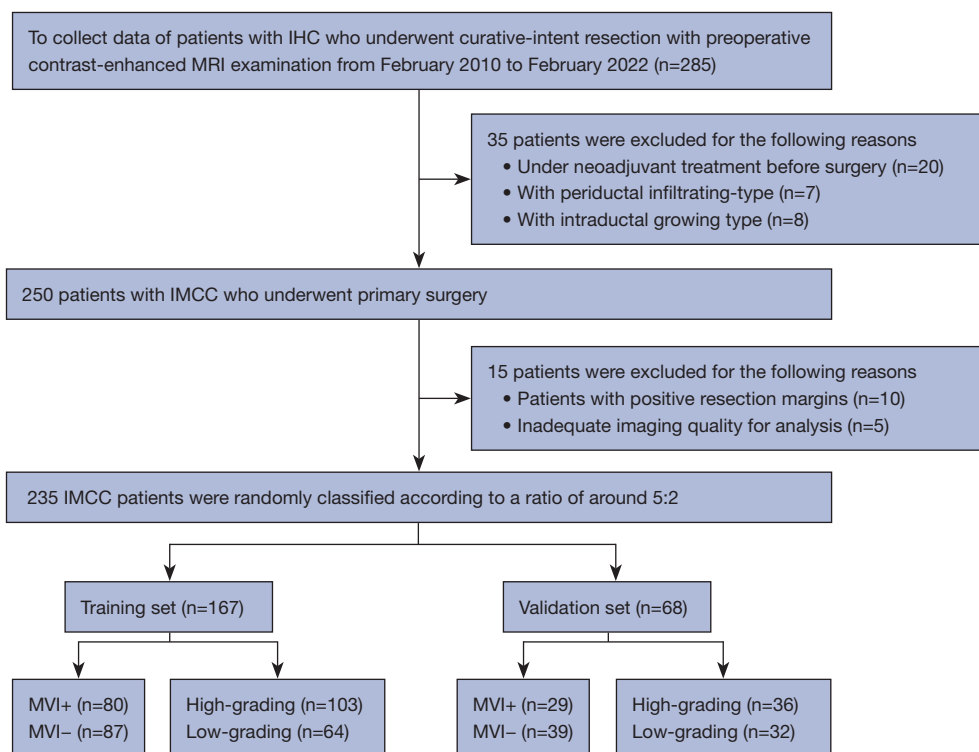
Figure 1 Flow diagram showing the patient selection protocol and the inclusion and exclusion criteria. IHC, intrahepatic cholangiocarcinoma; MRI, magnetic resonance imaging; IMCC, intrahepatic mass-forming cholangiocarcinoma; MVI, microvascular invasion.

analysis was waived.

Eligibility criteria and patients

A total of 285 consecutive IHC patients who underwent hepatic resection at the Chinese Academy of Medical Sciences and Peking Union Medical College were enrolled in the study from 1 February 2010 to 2 February 2022. The inclusion criteria were as follows: (I) patients with a pathological confirmation of IHC from liver resection specimens; and (II) patients who underwent a preoperative MRI examination before surgery at the Chinese Academy of Medical Sciences and Peking Union Medical College. The excluded patients met the following criteria: (I) patients under neoadjuvant treatment before surgery (n=20); (II) other types of IHC (n=15; 7 for periductal-infiltrating type and 8 for intraductal growing type); (III) patients with positive resection margins (n=10); and (IV) inadequate imaging quality for analysis (n=5). Ultimately, 235 eligible patients [median age, 60 years; interquartile range (IQR), 53–66; age range, 36–80 years; 146 men] were enrolled in our study and randomly divided into training

(n=167) and validation (n=68) cohorts at a ratio of around 5:2 (*Figure 1*). The same cohort was used to predict both MVI status and tumor grading. The median time between the MRI examination and hepatectomy was 15 days (IQR, 9–21 days). The tumor specimens of all patients were obtained through pathological detection for MVI and tumor grading postoperatively.

MRI protocols

MRI examinations were acquired with 8-channel phased array coil 3.0-T MRI scanners (Discovery MR 750 for 43 patients, SIGNA Excite HDxt for 92 patients, SIGNA Pioneer for 46 patients, and SIGNA Architect for 25 patients; GE Healthcare, Waukesha, WI, USA; Magnetom Spectra for 17 patients, and Magnetom Prisma for 12 patients; Siemens, Erlangen, Germany). The patients fasted for at least 4 hours before examination. All patients underwent routine abdominal MRI performed using the following sequences: non-CE T1-weighted in-phase and opposed-phase, T2 weighted imaging-fat-suppressed (T2WI-FS) on transverse, and T2WI on coronal. Diffusion-

weighted imaging (DWI) was obtained at b values of 0 and 800 s/mm^2. A total of 157 patients received 0.2 mmol/kg body weight of extracellular gadolinium contrast agent (Magnevist; Bayer AG, Leverkusen, Germany) at an infusion rate of 1.5–2 mL/s; the other patients received gadoxetic acid (Primovist; Bayer AG) injected at a dose of 0.025 mmol/kg at an infusion rate of 1 mL/s. Both were followed by a wash with 20 mL of 0.9% physiological saline flush, after which multiphasic dynamic images were obtained. The images in the arterial phase (AP), portal venous phase (PVP), and delayed phase (DP; for extracellular gadolinium contrast agents) or transitional phase (for gadoxetic acid) were acquired during suspended respiration at 25–35, 60–75, and 150–180 s, respectively, on transverse. Additionally, the hepatobiliary phase was acquired 10–15 minutes after the injection of gadoxetate disodium. For patients with cirrhosis, a 20-minute hepatobiliary phase is preferred. The last phase was scanned in the coronal direction after the transverse scan. Detailed technical specifications are shown in Table S1.

Preoperative information collecting

Preoperative information mainly included 20 items that were categorized into the following groups: (I) the standard demographics of the patients (including age and sex); (II) 7 laboratory variables, including hepatitis Be antigen (HBeAg), α-fetoprotein (AFP), carbohydrate antigen 19-9 (CA19-9), carcinoembryonic antigen (CEA), alanine aminotransferase (ALT), aspartate aminotransferase (AST), and gamma-glutamyl transpeptidase (GGT); and (III) 11 MRI morphological features, including tumor maximum diameter, number of tumors, tumor margin, necrosis, bile duct dilatation, capsule retraction, peritumoral enhancement, DWI signal characteristics, AP enhancement patterns, targetoid appearance, and lymph node status. The detailed classifications and definitions of each MRI feature are shown in Table S2. All MRI features were independently evaluated on a picture archiving and communication system by 2 radiologists (radiologists 1 and 2, with 10 and 8 years of experience in abdominal imaging, respectively). Any discrepancy was discussed to reach a final consensus.

Radiomic feature extraction

Radiomics features were extracted from T2WI-FS and DWI (b=800 s/mm^2) sequences. Both sequences were resampled and aligned to the same resolution, spacing, and position by ITK-SNAP (http://www.itksnap.org) to offset the interference caused by the uneven spatial resolution. The trilinear interpolation algorithm was used to resample the T2WI/FS and DWI with a new image resolution of 1 mm × 1 mm × 1 mm. Tumor volumes of interest (VOIs) covering the total volume of tumor tissue (hyperintense signal intensity on T2WI-FS, and restricted diffusion on DWI) were manually segmented by radiologist 1 on transverse slices using ITK-SNAP. VOIs also included cystic necrotic regions, which are considered one of the manifestations of tumor biological behaviors (21). The original MRI images and VOIs were saved as medical digital imaging files in Neuroimaging Informatics Technology Initiative (NII) format. To assess the intraobserver repeatability and reliability of the extracted features, 70 patients (approximately 30% of the total patients) were randomly selected, and the same segmentation procedure was repeated 1 month after the first evaluation by the same radiologist to reduce recall bias. The intraclass correlation coefficient (ICC) was used to assess the reproducibility of the radiomics features (22). All image segmentations were reviewed by radiologist 2. The PyRadiomics software package (version 3.0.1; http://www.radiomics.io/pyradiomics.html) was used to extract radiomics features from VOIs (23). The radiomics features were obtained on the original images using the wavelet and Laplacian of Gaussian filters with sigma values of 1.0, 2.0, 3.0, 4.0, and 5.0. A single-level directional discrete wavelet transform with high-pass (H) and low-pass (L) filters was used for wavelet transform (24). In total, 8 wavelet-decomposition images were created from each MRI sequence input, including HHH, HHL, HLH, HLL, LHH, LHL, LLH, and LLL. Finally, we extracted 1,132 radiomic features, including first-order statistical features (234 features), shape features (14 features), gray-level co-occurrence matrix (GLCM) features (286 features), gray-level run-length matrix (GLRLM) features (208 features), gray-level size zone matrix (GLSZM) features (208 features), and gray-level dependence matrix (GLDM) features (182 features), from the original images and wavelet-transformed images. In the process of MRI characteristic evaluation and VOI delineation, both radiologists were aware of the diagnosis of IMCC but were blinded to the clinicopathologic traits. For multinodular tumors (including satellite nodules and intrahepatic metastasis), only the targeted lesion (the largest nodule) was selected for further analysis. The average time needed for segmentation was
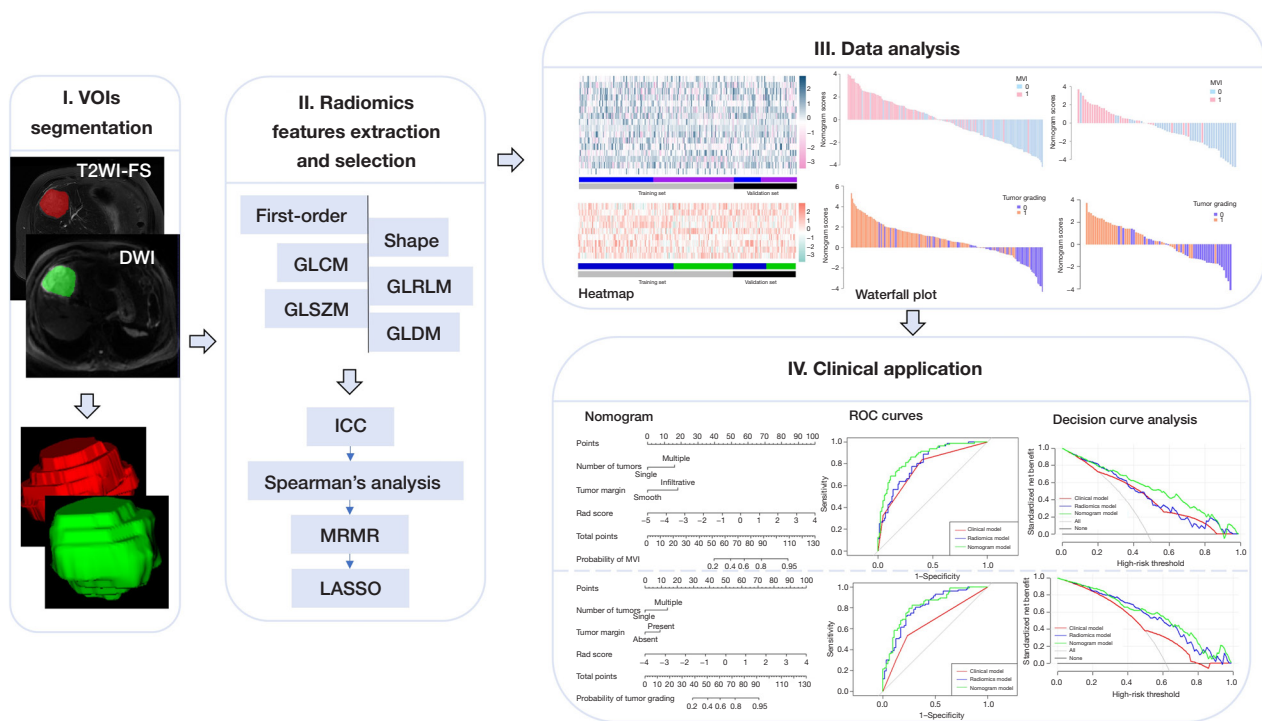
Figure 2 Radiomics pipeline of the study. VOI, volume of interest; T2WI-FS, T2 weighted imaging-fat-suppressed; DWI, diffusion-weighted images; GLCM, gray-level co-occurrence matrix; GLSZM, gray-level size zone matrix; GLRLM, gray-level run-length matrix; GLDM, gray-level dependence matrix; ICC, intraclass correlation coefficient; MRMR, minimum redundancy maximum relevance; LASSO, least absolute shrinkage and selection operator; MVI, microvascular invasion; ROC, receiver operating characteristic.

7 minutes (range, 4–10 minutes). The radiomics workflow is depicted in *Figure 2*.

Feature selection

The VOIs were saved as label maps and then used to obtain the radiomics features. To render the parameters of different dimensions comparable, the values of the extracted features in the training set were normalized by the *Z* score, and the mean and standard deviation (SD) values based on the training set were used to standardize the values of the validation set. We followed a 4-step procedure to identify robust radiomic features (Figure S1). First, we used ICC to evaluate the repeatability of radiomics features. The features with ICC ≥0.8 were chosen as having high reproducibility for further analysis and the other features were discarded as low reproducibility. Second, Spearman's analysis was used to calculate the correlation between radiomics features in a single sequence (T2WI/FS or DWI). Features with |ρ| ≥0.9 were defined as highly correlated. If correlation factor was high, any of the features were randomly selected

for further analysis, and the other features were discarded. Third, minimum redundancy maximum relevance (MRMR) was used to remove the redundant and irrelevant features in the training set (30 features were retained). Finally, we used least absolute shrinkage and selection operator (LASSO) regression in the training set to select the optimized features with nonzero coefficients with 10-fold cross-validation.

Models construction and evaluation

The clinical data, and MRI morphological features were subsequently compared by univariate logistic analysis. The clinical data included the standard demographics of the patients (age and sex), and laboratory variables (HBeAg, AFP, CA19-9, CEA, ALT, AST, and GGT). Significant features with P values <0.05 were included in the multivariable logistic regression analysis. The clinical models were established based on significant features of demographics, laboratory, and MRI morphological features. The radiomics models were built based on the selected radiomics features. Then, the rad_score of each patient was calculated based

8084

Chen et al. Prediction of MVI and tumor grading

on a linear combination of the selected features with the coefficients weighted by the LASSO regression. The independent features in the clinical models and rad_scores were combined to establish nomogram models for the prediction of MVI and tumor grading, respectively. The validation group was used to test the internal validation of the nomograms. A nomogram score was calculated for each patient in the training and validation sets.

Performance and validation of the prediction model

The areas under the receiver operating characteristic (ROC) curve (AUCs) were used to predict the accuracy of each model. The difference in the ROC curves between various models were assessed by the DeLong test. The sensitivity, specificity, and positive predictive value (PPV), and negative predictive value (NPV) of the predictive models were calculated by cross-tabulation. The model calibration was assessed by using calibration curves with the Hosmer-Lemeshow test. Additionally, decision curve analysis (DCA) was used to evaluate the clinical utility of the prediction model by computing the net benefits for a range of threshold probabilities.

Histopathologic analysis

The pathological examination results were recorded according to the hospital clinical records. The pathological slices of IMCC were subjected to postoperative hematoxylin and eosin (H&E) staining. MVI was defined as the presence of nested clusters of cancer cells within the endothelium-covered vessels diagnosed only by microscopy (25). The histologic grading of IMCC was divided into 3 categories: G1 (well differentiated), G2 (moderately differentiated), and G3 (poorly differentiated) (26). In our study, we defined G1 and/or G2 as "low grading" and G3 as "high grading".

Statistical analysis

Clinical, histopathologic, and MRI morphological features are expressed as numbers (frequency %) or the mean ± SD as appropriate. The Mann-Whitney U test or unpaired t-test was used for continuous variables according to the normal distribution test, and the chi-square test or Fisher's exact test was used for categorical variables. Interobserver agreement was analyzed for each qualitative MRI feature by the κ statistic. The level of agreement was assessed as slight (κ of 0.01 to 0.20), fair

(0.21 to 0.40), moderate (0.41 to 0.60), good (0.61 to 0.80), and excellent (0.81 to 1). Associated odds ratios (ORs) and 95% confidence intervals (CIs) were estimated. Statistical significance was defined as P values <0.05 (2-tailed). Statistical analysis was carried out by SPSS 23.0 (IBM Corp., Armonk, NY, USA) and R statistical software (version 4.0.3, https://www.r-project.org).

Results

Interobserver agreements

The percentage of MRI morphological features identified for feature classification by the 2 radiologists as well as their interobserver agreements for each imaging feature are shown in Table S3. The κ values for MRI morphological features were good to excellent (κ=0.634–0.888).

Clinical and MRI characteristics of the patients

A total of 235 patients were enrolled in this study, among whom 167 patients (MVI+ =80, MVI− =87; high grading =103, low grading =64) were enrolled in the training set. In the validation set, 68 patients were enrolled, including 29 patients with MVI+, 39 with MVI−, 36 with high grading and 32 with low grading, showing no significant difference in tumor pathological behaviors in the distribution among patients (P=0.464 for MVI; P=0.217 for tumor grading). Additionally, there were no significant differences in clinical and MRI characteristics between the training and validation sets except for AFP (P=0.014). The demographic and tumor characteristics are summarized in *Table 1*.

Selection of predictive factors

In univariable logistic regression analysis, 6 and 2 variables were significantly associated with an increased risk for MVI and tumor grading, respectively (*Table 2*). Multivariable logistic regression analysis identified number of tumors (P=0.002, OR =4.590, 95% CI: 1.736–12.136) and tumor margin (P<0.001, OR =5.472, 95% CI: 2.538–11.797) as independent predictors of MVI. For tumor grading, number of tumors (P=0.022, OR =2.752, 95% CI: 1.201–5.947) and tumor necrosis (P=0.016, OR =2.156, 95% CI: 1.157–6.547) were identified as independent risk factors in multivariable logistic regression analysis (*Table 2*). These independent risk factors were used for clinical models' construction for the prediction of MVI and tumor grading.

Table 1 Clinical and radiological characteristics in the training and validation sets

Variables	Training set (n=167)						Validation set (n=68)						P-Inter value
	MVI (+), n=80	MVI (−), n=87	P-Intra value	High grade, n=103	Low grade, n=64	P-Intra value	MVI (+), n=29	MVI (−), n=39	P-Intra value	High grade, n=36	Low grade, n=32	P-Intra value	
Age (year)[†]	59±9.7	60±8.7	0.833	59±9.6	59±8.7	0.890	59.0±9.2	60.3±8.9	0.539	58.8±8.5	61.1±9.6	0.621	0.120
Sex			0.328			0.916			0.841			0.773	0.266
Male	51 (63.8)	49 (56.3)		62 (60.2)	38 (59.4)		20 (69.0)	26 (66.7)		27 (75.0)	19 (59.4)		
Female	29 (36.2)	38 (43.7)		41 (39.8)	26 (40.6)		9 (31.0)	13 (33.3)		9 (25.0)	13 (40.6)		
HBsAg			0.965			0.053			0.904			0.511	0.662
Positive	26 (32.5)	28 (32.2)		39 (37.9)	15 (23.4)		10 (34.5)	14 (35.9)		14 (38.9)	10 (31.2)		
Negative	54 (67.5)	59 (67.8)		64 (62.1)	49 (76.6)		19 (65.5)	25 (64.1)		22 (61.1)	22 (68.8)		
CA19-9, U/mL			0.028			0.477			0.013			0.219	0.400
>37	53 (66.2)	43 (49.4)		57 (55.3)	39 (60.9)		20 (69.0)	15 (38.5)		16 (44.4)	19 (59.4)		
≤37	27 (33.8)	44 (50.6)		46 (44.7)	25 (39.1)		9 (31.0)	24 (61.5)		20 (55.6)	13 (40.6)		
AFP, ng/mL			0.200			0.834			−			−	0.014
>20	9 (11.2)	5 (5.7)		9 (8.7)	5 (7.8)		0 (0)	0 (0)		0 (0)	0 (0)		
≤20	71 (88.8)	82 (94.3)		94 (91.3)	59 (92.2)		29 (100.0)	39 (100.0)		36 (100.0)	32 (100.0)		
CEA, ng/mL			0.051			0.182			0.721			0.931	0.852
>5	22 (27.5)	13 (14.9)		25 (24.3)	10 (15.6)		7 (24.1)	8 (20.5)		8 (22.2)	7 (21.9)		
≤5	58 (72.5)	74 (85.1)		78 (75.7)	54 (84.4)		22 (75.9)	31 (79.5)		28 (77.8)	25 (78.1)		
ALT, U/L			0.753			0.796			0.887			0.575	0.373
>40	15 (18.7)	18 (20.7)		21 (20.4)	12 (18.7)		7 (24.1)	10 (25.6)		10 (27.8)	7 (21.9)		
≤40	65 (81.3)	69 (79.3)		82 (79.6)	52 (81.3)		22 (75.9)	29 (74.4)		26 (72.2)	25 (78.1)		
AST, U/L			0.534			0.672			0.940			0.092	0.695
>40	11 (13.7)	15 (17.2)		17 (16.5)	9 (14.1)		5 (17.2)	7 (17.9)		9 (25.0)	3 (9.4)		
≤40	69 (86.3)	72 (82.8)		86 (83.5)	55 (85.9)		24 (82.8)	32 (82.1)		27 (75.0)	29 (90.6)		
GGT			0.088			0.125			0.025			0.726	0.979
>55	37 (46.2)	29 (33.3)		36 (35.0)	30 (46.9)		16 (55.2)	11 (28.2)		15 (41.7)	12 (37.5)		
≤55	43 (53.8)	58 (66.7)		67 (65.0)	34 (53.1)		13 (44.8)	28 (71.8)		21 (58.3)	20 (62.5)		
Tumor diameter, cm			0.009			0.051			0.418			0.100	0.139
>5	51 (63.8)	38 (43.7)		61 (59.2)	28 (43.7)		14 (48.3)	15 (38.5)		12 (33.3)	17 (53.1)		
≤5	29 (36.2)	49 (56.3)		42 (40.8)	36 (56.3)		15 (51.7)	24 (61.5)		24 (66.7)	15 (46.9)		
Numbers of tumor			0.001			0.009			0.022			0.109	0.081
Single	49 (61.3)	79 (90.8)		72 (69.9)	56 (87.5)		22 (75.9)	37 (94.9)		29 (80.6)	30 (93.8)		
Multiple	31 (38.7)	8 (9.2)		31 (30.1)	8 (12.5)		7 (24.1)	2 (5.1)		7 (19.4)	2 (6.2)		
Tumor margin			<0.001			0.397			0.002			0.438	0.858
Infiltrative	62 (77.5)	31 (35.6)		60 (58.3)	33 (51.6)		22 (75.9)	15 (38.5)		18 (50.0)	19 (59.4)		
Smooth	18 (22.5)	56 (64.4)		43 (41.7)	31 (48.4)		7 (24.1)	24 (61.5)		18 (50.0)	13 (40.6)		

Table 1 (*continued*)

Table 1 (*continued*)

Variables	Training set (n=167)						Validation set (n=68)						P-Inter value
	MVI (+), n=80	MVI (−), n=87	P-Intra value	High grade, n=103	Low grade, n=64	P-Intra value	MVI (+), n=29	MVI (−), n=39	P-Intra value	High grade, n=36	Low grade, n=32	P-Intra value	
Necrosis			0.304			0.007			0.841			<0.001	0.461
Absent	55 (68.8)	66 (75.9)		67 (65.0)	54 (84.4)		20 (69.0)	26 (66.7)		17 (47.2)	29 (90.6)		
Present	25 (31.2)	21 (24.1)		36 (35.0)	10 (15.6)		9 (31.0)	13 (33.3)		19 (52.8)	3 (9.4)		
Bile duct dilatation			0.301			0.713			0.106			0.557	0.104
Absent	52 (65.0)	63 (72.4)		72 (69.9)	43 (67.2)		17 (58.6)	30 (76.9)		26 (72.2)	21 (65.6)		
Present	28 (35.0)	24 (27.6)		31 (30.1)	21 (32.8)		12 (41.4)	9 (23.1)		10 (27.8)	11 (34.4)		
Hepatic capsule retraction			0.292			0.398			0.240			0.193	0.240
Absent	19 (23.7)	27 (31.0)		26 (25.2)	20 (31.2)		10 (34.5)	19 (48.7)		18 (50.0)	11 (34.4)		
Present	61 (76.3)	60 (69.0)		77 (74.8)	44 (68.8)		19 (65.5)	20 (51.3)		18 (50.0)	21 (65.6)		
Peritumoral enhancement			0.586			0.979			0.322			0.575	0.232
Absent	52 (65.0)	60 (69.0)		69 (67.0)	43 (67.2)		20 (69.0)	31 (79.5)		28 (77.8)	23 (71.9)		
Present	28 (35.0)	27 (31.0)		34 (33.0)	21 (32.8)		9 (31.0)	8 (20.5)		8 (22.2)	9 (28.1)		
DWI signal characteristics			0.526			0.107			0.583			0.702	0.441
Diffuse hypo-enhancement	37 (46.2)	36 (41.4)		40 (38.8)	33 (51.6)		10 (34.5)	16 (41.0)		13 (36.1)	13 (40.6)		
Diffuse hyper-enhancement	43 (53.8)	51 (58.6)		63 (61.2)	31 (48.4)		19 (65.5)	23 (59.0)		23 (63.9)	19 (59.4)		
AP enhancement pattern			0.234			0.001			0.014			0.910	0.338
Diffuse hypo-enhancement	13 (16.3)	9 (10.3)		11 (10.7)	11 (17.2)		9 (31.0)	3 (7.7)		7 (19.4)	5 (15.6)		
Rim-enhancement	60 (75.0)	64 (73.6)		83 (80.6)	41 (64.1)		18 (62.1)	26 (66.7)		23 (63.9)	21 (65.6)		
Diffuse hyper-enhancement	7 (8.7)	14 (16.1)		9 (8.7)	12 (18.7)		2 (6.9)	10 (25.6)		6 (16.7)	6 (18.8)		
Targetoid appearance			0.864			0.069			0.734			0.586	0.667
Absent	13 (16.3)	15 (17.2)		13 (12.6)	15 (23.4)		5 (17.2)	8 (20.5)		6 (16.7)	7 (21.9)		
Present	67 (83.7)	72 (82.8)		90 (87.4)	49 (76.6)		24 (82.8)	31 (79.5)		30 (83.3)	25 (78.1)		
Lymph node status			0.012			0.104			0.003			0.147	0.098
Positive	35 (43.7)	22 (25.3)		40 (38.8)	17 (26.6)		12 (41.4)	4 (10.3)		11 (30.6)	5 (15.6)		
Negative	45 (56.3)	65 (74.7)		63 (61.2)	47 (73.4)		17 (58.6)	35 (89.7)		25 (69.4)	27 (84.4)		
Rad_score, median (interquartile range)	0.639 (−0.122, 1.678)	−1.102 (−1.834, 0.221)	<0.001	1.132 (0.472, 1.921)	−0.258 (−1.246, 0.595)	<0.001	0.661 (−0.012, 1.765)	−0.922 (−1.380, 0.548)	<0.001	1.214 (0.668, 1.597)	−0.169 (−0.566, 0.879)	<0.001	–

Categorical variables are expressed as frequency with percentages in parentheses. [†], the mean ± standard deviation. Qualitative variables are analyzed using Pearson's χ^2 test or Fisher's exact test as appropriate, and quantitative variables are analyzed using the independent *t*-test. P-Intra is the result of univariate analyses between the MVI+ and MVI− groups, high-grade and low-grade groups; P-Inter value represents the comparisons of characteristics between training and validation set. MVI, microvascular invasion; HBsAg, hepatitis Be antigen; CA19-9, carbohydrate antigen 19-9; AFP, α-fetoprotein; CEA, carcinoembryonic antigen; ALT, alanine aminotransferase; AST, aspartate aminotransferase; GGT, gamma-glutamyl transpeptidase; DWI, diffusion-weighted imaging; AP, arterial phase; rad_score, radiomics score.

Table 2 Univariate and multivariable logistic regression analyses for selecting clinical and radiological features of model development of the training set

Variables	Univariate analysis		Multivariate analysis	
	Odds ratio (95% CI)	P value	Odds ratio (95% CI)	P value
MVI-status				
CA19-9 (>37 *vs.* ≤37 U/mL)	2.009 (1.074–3.755)	0.029*	1.245 (0.566–2.742)	0.586
CEA (>5 *vs.* ≤5 ng/mL)	2.159 (1.003–4.649)	0.049*	1.216 (0.479–3.082)	0.681
Tumor diameter (>5 *vs.* ≤5 cm)	2.268 (1.217–4.225)	0.010*	1.198 (0.553–2.598)	0.647
Number of tumors (multiple *vs.* single)	6.247 (2.657–14.691)	<0.001*	4.590 (1.736–12.136)	0.002*
Tumor margin (infiltrative *vs.* smooth)	6.222 (3.140–12.331)	<0.001*	5.472 (2.538–11.797)	<0.001*
Lymph node status (positive *vs.* negative)	2.314 (1.200–4.464)	0.012*	1.182 (0.522–2.680)	0.688
Tumor grading				
Numbers of tumor (multiple *vs.* single)	3.014 (1.285–7.066)	0.011*	2.752 (1.201–5.947)	0.022*
Necrosis (present *vs.* absent)	2.901 (1.321–6.374)	0.008*	2.156 (1.157–6.547)	0.016*

*, P<0.05. CI, confidence interval; MVI, microvascular invasion; CA19-9, carbohydrate antigen 19-9; CEA, carcinoembryonic antigen.

Feature selection and construction of radiomics models

Each MRI sequence contained 1,132 features, for a total of 2,264 features (T2WI-FS and DWI). Finally, 16 radiomics features (11 from T2WI-FS, 5 from DWI) for MVI prediction and 9 radiomics features (6 from T2WI-FS, 3 from DWI) for tumor grading detection were selected with nonzero coefficients with optimal regulation weights λ of 0.0398 and 0.0588, respectively, under the 1-SE criterion, and rad_scores were constructed (*Figure 3*). The selected radiomics features and their corresponding coefficients are detailed in Table S4. Figure S2 shows the heatmap of the selected radiomics features and scatter plots of the rad_scores for the MVI and tumor grading of IMCC in the training and validation sets. These represent the values of the rad_scores for all patients. The rad_scores showed statistically significant differences between MVI+ and MVI– and between high grading and low grading in the training and validation sets (all P<0.001) (*Table 1*). The rad_score yielded AUCs of 0.806 (95% CI: 0.742–0.870) in the training set and 0.783 (95% CI: 0.674–0.893) in the validation set for the prediction of MVI. For the prediction of tumor grading, the AUCs were 0.806 (95% CI: 0.737–0.874) and 0.779 (95% CI: 0.664–0.894) in the training and validation sets, respectively (*Table 3*).

Performance and comparison of the nomograms

Nomograms were constructed by incorporating significant MRI features and the rad_scores (*Figure 4*). All of the calibration curves for the nomograms showed that the predicted probabilities of the nomogram were closely aligned with the actual MVI and tumor grading estimates, with P values of 0.895 and 0.451 in the training set, respectively (Figure S3). The AUCs of the nomogram for predicting MVI were 0.874 (95% CI: 0.822–0.926) for the training set and 0.869 (95% CI: 0.783–0.955) for the validation set, whereas the AUCs of the nomogram for predicting tumor grading were 0.827 (95% CI: 0.763–0.891) for the training set and 0.848 (95% CI: 0.759–0.937) for the validation set (*Table 3*). Furthermore, the nomograms had significantly higher AUCs than the clinical models in both the training set (MVI, 0.874 *vs.* 0.787, P<0.001; tumor grading, 0.827 *vs.* 0.650, P<0.001) and validation set (MVI, 0.869 *vs.* 0.738, P=0.008; tumor grading, 0.848 *vs.* 0.734, P=0.002) for the prediction of both MVI and tumor grading (*Figure 5*, Table S5). The AUC difference between each model is provided in Table S5. The nomogram score for each patient is shown in Figure S4. The corresponding accuracy, sensitivity, specificity, PPV, and NPV are presented in *Table 3*.

Clinical utility

DCA was performed for the nomograms for predicting the presence of MVI and tumor grading, which reflected that the clinical utility and was presented in the training set. As
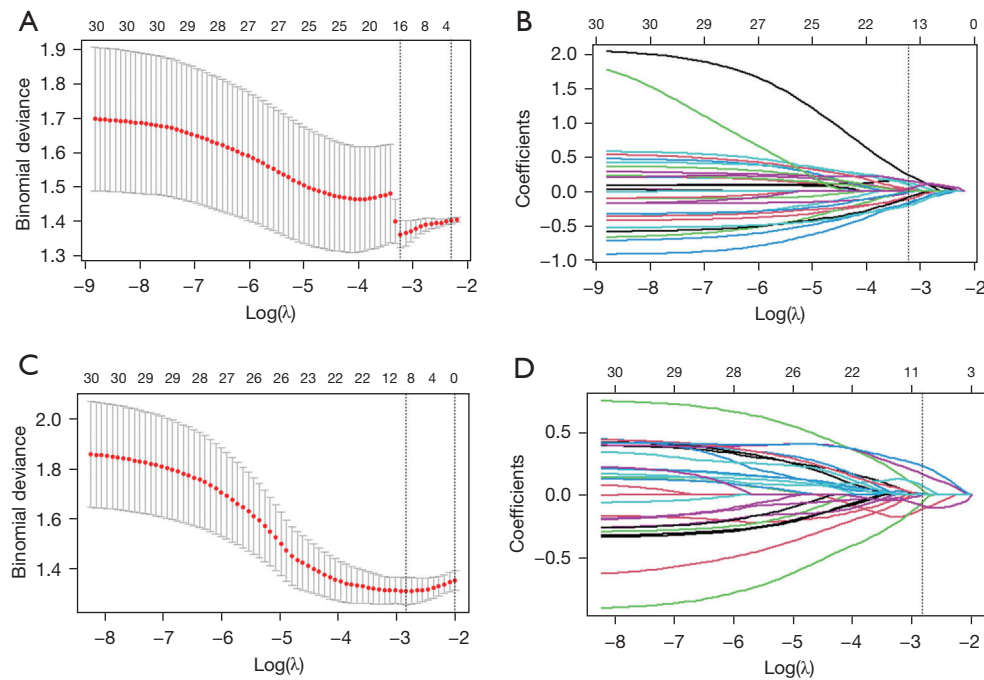
Figure 3 Feature selection with the LASSO regression model. The LASSO model's tuning parameter (λ) selection used 10-fold cross-validation via minimum criterion (A) and (C). Dotted vertical lines were drawn at the optimal values by using the minimum criteria and the 1 standard error of the minimum criteria (the 1-SE criteria). LASSO coefficient profile plot with different log (λ) was shown. The vertical dashed lines represent 16 radiomics features for MVI prediction (B) and 9 radiomics features for tumor grading prediction (D) with nonzero coefficients selected with the optimal λ value. LASSO, least absolute shrinkage and selection operator; MVI, microvascular invasion.

shown in Figure S5, using the nomogram and rad_scores for MVI prediction added more benefit than using the "treat-all strategy" or "treat-none strategy" within a certain range of thresholds (the range of the radiomics model and nomogram was between 10% and 95%). Similar results were found in the prediction of tumor grading (radiomics model, between 10% and 95%; nomogram, >10%).

Discussion

In our study, we constructed 2 nomograms incorporating the rad_scores and MRI morphological risk factors for the prediction of MVI and tumor grading of IMCC. Our findings demonstrated that the radiomics features and MRI morphological features had an acceptable ability to discriminate the pathological features of the tumor. The calibration curves and DCA showed the good clinical utility of these easy-to-use nomogram prediction models for MVI and tumor grading.

The rad_scores based on T2WI-FS and DWI showed better performance outcomes (AUCs of 0.783 and 0.806,

respectively) in the prediction of MVI than the clinical model (AUCs of 0.787 and 0.738, respectively) in the study. The nomogram combining rad_scores and significant MRI morphological features had the highest diagnostic performance for the prediction of MVI, with AUCs of 0.874 and 0.869 in the training and validation sets, respectively. Zhou et al. (20) utilized a set of 7 wavelet features based on gadolinium ethoxybenzyl diethylenetriamine pentaacetic acid (Gd-DTPA)-enhanced MRI for the prediction of MVI, and the radiomics model reached AUCs of 0.850–0.873. Qian et al. (18) established a nomogram incorporating intrahepatic duct dilatation, tumor size, and rad_score (DWI, T2WI-FS, T1WI, AP, PVP, and DP) with an AUC range of 0.819 to 0.953, and the diagnostic performance was similar to that of our nomogram.

To date, to the best of our knowledge, no study has employed radiomics features based on MRI to predict tumor grading of IMCC. In our study, the radiomics model achieved AUCs of 0.806 and 0.779 in the training and validation sets, respectively, and the nomogram achieved the best predictive ability (AUCs of 0.827 and 0.848,

Table 3 Diagnostic performance of different models for predicting MVI and tumor grade in training and validation sets

Model	AUC	Accuracy, %	Sensitivity, %	Specificity, %	PPV, %	NPV, %
MVI						
Training set						
Clinical model	0.787 (0.716, 0.857)	71.26 (63.76, 77.99)	83.75 (73.82, 91.05)	59.77 48.71, 70.15)	65.69 (55.63, 74.81)	80.00 (68.23, 88.90)
Radiomics model	0.806 (0.742, 0.870)	71.26 (63.76, 77.99)	71.25 (60.05, 80.82)	71.26 (60.57, 80.46)	69.51 (58.36, 79.20)	72.94 (62.21, 82.01)
Nomogram model	0.874 (0.822, 0.926)	77.25 (70.13, 83.37)	73.75 (62.71, 82.96)	80.46 (70.57, 88.19)	77.63 (66.62, 86.40)	76.92 (66.91, 85.11)
Validation set						
Clinical model	0.738 (0.618, 0.858)	69.12 (56.74, 79.76)	82.76 (64.23, 94.15)	58.97 (42.10, 74.43)	60.00 (43.33, 75.14)	82.14 (63.11, 93.93)
Radiomics model	0.783 (0.674, 0.893)	69.12 (56.74, 79.76)	62.07 (42.26, 79.31)	74.36 (57.87, 86.96)	64.29 (44.06, 81.36)	72.50 (56.11, 85.40)
Nomogram model	0.869 (0.783, 0.955)	79.41 (67.88, 88.26)	75.86 (56.46, 89.70)	82.05 (66.47, 92.46)	75.86 (56.46, 89.70)	82.05 (66.47, 92.46)
Tumor grading						
Training set						
Clinical model	0.650 (0.565, 0.734)	63.47 (55.68, 70.78)	55.34 (45.22, 65.14)	76.56 (64.31, 86.25)	79.17 (67.98, 87.84)	51.58 (41.10, 61.96)
Radiomics model	0.806 (0.737, 0.874)	74.25 (66.92, 80.70)	85.44 (77.12, 91.61)	56.25 (43.28, 68.63)	75.86 (67.04, 83.32)	70.59 (56.17, 82.51)
Nomogram model	0.827 (0.763, 0.891)	76.65 (69.49, 82.84)	85.44 (77.12, 91.61)	62.50 (49.51, 74.30)	78.57 (69.81, 85.76)	72.73 (59.04, 83.86)
Validation set						
Clinical model	0.734 (0.614, 0.854)	70.59 (58.29, 81.02)	58.33 (40.76, 74.49)	84.38 (67.21, 94.72)	80.77 (60.65, 93.45)	64.29 (48.03, 78.45)
Radiomics model	0.779 (0.664, 0.894)	72.06 (59.85, 82.26)	80.56 (63.98, 91.81)	62.50 (43.69, 78.90)	70.73 (54.46, 83.87)	74.07 (53.71, 88.89)
Nomogram model	0.848 (0.759, 0.937)	73.52 (61.42, 83.50)	77.78 (60.85, 89.88)	68.75 (49.99, 83.88)	73.68 (56.90, 86.60)	73.33 (54.11, 87.72)

Data in parentheses are 95% confidence intervals. MVI, microvascular invasion; AUC, area under the receiver operating characteristic curve; PPV, positive predictive value; NPV, negative predictive value.

respectively). Rad_scores based on positron emission tomography/computed tomography (PET/CT) (27) and ultrasound (28) have been used to preoperatively predict tumor grading, with AUCs ranging from 0.71 to 0.78. However, the case number was limited (74 to 128 patients) and a validation test was lacking, which may have led to a possible risk of data overfitting. We hypothesized that the radiomics features of MRI are superior to those of other

examination devices, but further validation is needed.

MRMR is used to select radiomics features that can provide less redundancy and more reliable coefficients in the classifier (29). In addition, the LASSO method is an excellent approach for feature screening, obtaining good features of both ridge regression and subset screening and enabling the panel of selected features to be combined into rad_scores (30). Therefore, optimal radiomics features were
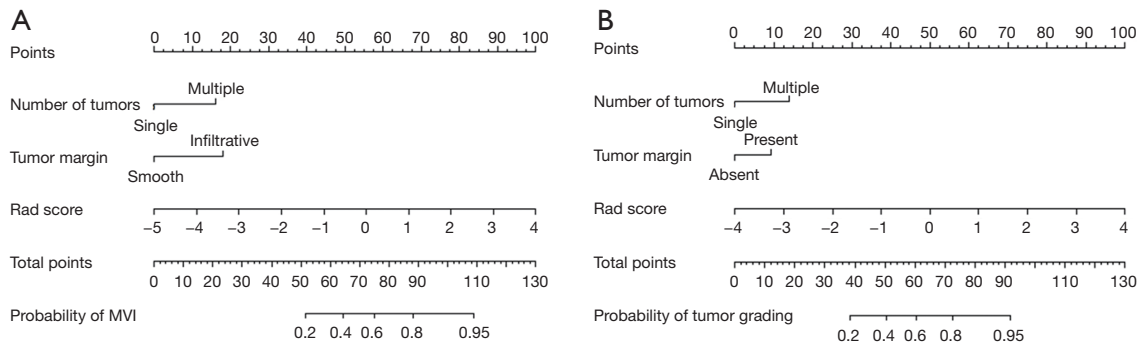
Figure 4 Development of nomograms. (A) The nomogram to predict MVI developed from tumor number, tumor margin status and radiomics signature (rad_score) of the training set. (B) The nomogram to predict high tumor grade developed from the tumor number, necrosis and rad_score of the training set for intrahepatic mass-forming cholangiocarcinoma. MVI, microvascular invasion.
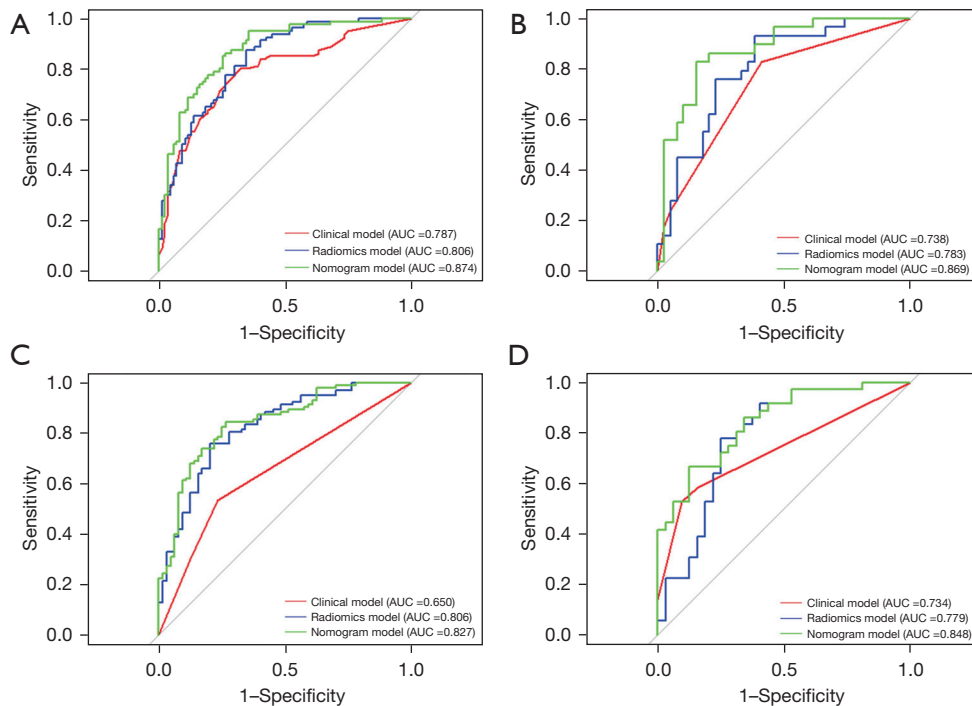
Figure 5 ROC curves. Graph shows the receiver operating characteristic curve of the radiomic model (blue), clinical model (red), and nomogram model (green) for MVI differentiation, for the training (A) and validation set (B). The ROC curves of the radiomic model (blue), clinical model (red), and nomogram model (green) for tumor grading prediction, for the training (C) and validation set (D), respectively. AUC, area under the receiver operating characteristic curve; ROC, receiver operating characteristic; MVI, microvascular invasion.

selected in this way in our study. Alternatively, it is worth mentioning that the radiomics features extracted from T2WI-FS (11/16 for MVI and 6/9 for tumor grading) and wavelet features (11/16 for MVI and 6/9 for tumor grading) exhibited higher weights in the rad_scores. These results showed that wavelet transformation can further reflect the

spatial heterogeneity across multiple dimensions, which is consistent with previous studies (31,32). We also assume that radiomics features extracted from T2WI-FS are more useful for predicting the aggressive behaviors of tumors than those extracted from DWI. This could be attributed to the fact that T2WI-FS has a higher signal-to-noise ratio, spatial

resolution, and image contrast than DWI images (33).

Multivariate logistic regression analysis showed that multiple tumors was an independent factor in the prediction of both MVI and tumor grading, which was consistent with previous studies (9,34,35). The presence of multiple tumors is a visible sign of invasiveness and an external manifestation of the tumor's poor biological behavior. Tumor margin is an important predictor of MVI. Xiang *et al.* (34) reported that a blurry or infiltrative contour of the tumor on CT is a significant risk factor for MVI. Our results concur with this report. Tumor necrosis is another important predictive factor associated with pathological grading in the study. A common hypothesis is that the rapid growth of malignant cells, especially in the more aggressive types of cancer, with the subsequent generation of hypoxic conditions, exceeds their own blood supply and leads to necrosis of tissue areas (36). The most reliable criterion for evaluating tumor necrosis is pathological diagnosis; therefore, radiographically assessing the degree of consistency of necrosis with pathological specimens requires validation.

Our study has several limitations. First, this was a retrospective study at a single institute and may have selection bias. Therefore, external validation is anticipated in the future through a public database through a multisite study to assess the practicability of the results. Second, we did not include contrast-enhanced (CE) sequences because the patients enrolled in our study used different liver contrast agents, including liver-specific contrast agents and extracellular contrast agents. Although the nomograms in our study obtained a favorable performance in the prediction of MVI and tumor grading, CE sequences, which would show further characteristics of IMCC, might contain more information and needs further analysis. Finally, this study was also limited by the heterogeneity of the MRI protocols, which were not standardized because of the retrospective design of the study.

Conclusions

The nomograms based on MRI radiomics features and morphological features may be helpful for preoperatively predicting MVI and tumor grading in IMCC, which may help clinicians to choose individual and optimal surgical strategies to improve clinical outcomes.

Acknowledgments

Footnote

References

1. Cerrito L, Ainora ME, Borriello R, Piccirilli G, Garcovich M, Riccardi L, Pompili M, Gasbarrini A, Zocco MA. Contrast-Enhanced Imaging in the Management of Intrahepatic Cholangiocarcinoma: State of Art and Future Perspectives. Cancers (Basel) 2023;15:3393.
2. Kupietzky A, Ariche A. Surgical Aspects of Intrahepatic Cholangiocarcinoma. Cancers (Basel) 2022;14:6265.
3. Razumilava N, Gores GJ. Cholangiocarcinoma. Lancet 2014;383:2168-79.
4. Guglielmi A, Ruzzenente A, Campagnaro T, Pachera S, Valdegamberi A, Nicoli P, Cappellani A, Malfermoni G, Iacono C. Intrahepatic cholangiocarcinoma: prognostic factors after surgical resection. World J Surg 2009;33:1247-54.

5. de Jong MC, Nathan H, Sotiropoulos GC, Paul A, Alexandrescu S, Marques H, et al. Intrahepatic cholangiocarcinoma: an international multi-institutional analysis of prognostic factors and lymph node assessment. J Clin Oncol 2011;29:3140-5.

6. Doussot A, Gonen M, Wiggers JK, Groot-Koerkamp B, DeMatteo RP, Fuks D, Allen PJ, Farges O, Kingham TP, Regimbeau JM, D'Angelica MI, Azoulay D, Jarnagin WR. Recurrence Patterns and Disease-Free Survival after Resection of Intrahepatic Cholangiocarcinoma: Preoperative and Postoperative Prognostic Models. J Am Coll Surg 2016;223:493-505.e2.

7. Xu X, Zhang HL, Liu QP, Sun SW, Zhang J, Zhu FP, Yang G, Yan X, Zhang YD, Liu XS. Radiomic analysis of contrast-enhanced CT predicts microvascular invasion and outcome in hepatocellular carcinoma. J Hepatol 2019;70:1133-44.

8. Atanasov G, Dietel C, Feldbrügge L, Benzing C, Krenzien F, Brandl A, Mann E, Englisch JP, Schierle K, Robson SC, Splith K, Morgul MH, Reutzel-Selke A, Jonas S, Pascher A, Bahra M, Pratschke J, Schmelzle M. Tumor necrosis and infiltrating macrophages predict survival after curative resection for cholangiocarcinoma. Oncoimmunology 2017;6:e1331806.

9. Chen Y, Liu H, Zhang J, Wu Y, Zhou W, Cheng Z, Lou J, Zheng S, Bi X, Wang J, Guo W, Li F, Wang J, Zheng Y, Li J, Cheng S, Zeng Y, Liu J. Prognostic value and predication model of microvascular invasion in patients with intrahepatic cholangiocarcinoma: a multicenter study from China. BMC Cancer 2021;21:1299.

10. Ji GW, Jiao CY, Xu ZG, Li XC, Wang K, Wang XH. Development and validation of a gradient boosting machine to predict prognosis after liver resection for intrahepatic cholangiocarcinoma. BMC Cancer 2022;22:258.

11. Jiang C, Zhao L, Xin B, Ma G, Wang X, Song S. (18) F-FDG PET/CT radiomic analysis for classifying and predicting microvascular invasion in hepatocellular carcinoma and intrahepatic cholangiocarcinoma. Quant Imaging Med Surg 2022;12:4135-50.

12. Erstad DJ, Tanabe KK. Prognostic and Therapeutic Implications of Microvascular Invasion in Hepatocellular Carcinoma. Ann Surg Oncol 2019;26:1474-93.

13. Lu WF, Chen PQ, Yan K, Wu YC, Liang L, Yuan JY, Fu Y, Zhang HB. Synergistic impact of resection margin and microscopic vascular invasion for patients with HBV-related intrahepatic cholangiocarcinoma. Expert Rev Gastroenterol Hepatol 2021;15:575-82.

14. Martin SP, Ruff S, Diggs LP, Drake J, Ayabe RI, Brown ZJ, Wach MM, Steinberg SM, Davis JL, Hernandez JM. Tumor grade and sex should influence the utilization of portal lymphadenectomy for early stage intrahepatic cholangiocarcinoma. HPB (Oxford) 2019;21:419-24.

15. Heimbach JK, Sanchez W, Rosen CB, Gores GJ. Trans-peritoneal fine needle aspiration biopsy of hilar cholangiocarcinoma is associated with disease dissemination. HPB (Oxford) 2011;13:356-60.

16. Ma X, Liu L, Fang J, Rao S, Lv L, Zeng M, Shi Y, Yang C. MRI features predict microvascular invasion in intrahepatic cholangiocarcinoma. Cancer Imaging 2020;20:40.

17. Zhou Y, Wang X, Xu C, Zhou G, Liu X, Gao S, Xu P. Mass-forming intrahepatic cholangiocarcinoma: Can diffusion-weighted imaging predict microvascular invasion? J Magn Reson Imaging 2019;50:315-24.

18. Qian X, Lu X, Ma X, Zhang Y, Zhou C, Wang F, Shi Y, Zeng M. A Multi-Parametric Radiomics Nomogram for Preoperative Prediction of Microvascular Invasion Status in Intrahepatic Cholangiocarcinoma. Front Oncol 2022;12:838701.

19. Lambin P, Leijenaar RTH, Deist TM, Peerlings J, de Jong EEC, van Timmeren J, Sanduleanu S, Larue RTHM, Even AJG, Jochems A, van Wijk Y, Woodruff H, van Soest J, Lustberg T, Roelofs E, van Elmpt W, Dekker A, Mottaghy FM, Wildberger JE, Walsh S. Radiomics: the bridge between medical imaging and personalized medicine. Nat Rev Clin Oncol 2017;14:749-62.

20. Zhou Y, Zhou G, Zhang J, Xu C, Wang X, Xu P. Radiomics signature on dynamic contrast-enhanced MR images: a potential imaging biomarker for prediction of microvascular invasion in mass-forming intrahepatic cholangiocarcinoma. Eur Radiol 2021;31:6846-55.

21. Li H, Wang L, Zhang J, Duan Q, Xu Y, Xue Y. Evaluation of microvascular invasion of hepatocellular carcinoma using whole-lesion histogram analysis with the stretched-exponential diffusion model. Br J Radiol 2022;95:20210631.

22. Koo TK, Li MY. A Guideline of Selecting and Reporting Intraclass Correlation Coefficients for Reliability Research. J Chiropr Med 2016;15:155-63. Erratum in: J Chiropr Med 2017;16:346.

23. van Griethuysen JJM, Fedorov A, Parmar C, Hosny A, Aucoin N, Narayan V, Beets-Tan RGH, Fillion-Robin JC, Pieper S, Aerts HJWL. Computational Radiomics System to Decode the Radiographic Phenotype. Cancer Res 2017;77:e104-7.

24. Wang JZ. Wavelets and imaging informatics: a review of

the literature. J Biomed Inform 2001;34:129-41.

25. Shao C, Chen J, Chen J, Shi J, Huang L, Qiu Y. Histological classification of microvascular invasion to predict prognosis in intrahepatic cholangiocarcinoma. Int J Clin Exp Pathol 2017;10:7674-81.

26. Washington MK, Berlin J, Branton PA, Burgart LJ, Carter DK, Compton CC, Frankel WL, Jessup JM, Kakar S, Minsky B, Nakhleh RE, Vauthey JN; . Protocol for the examination of specimens from patients with carcinoma of the intrahepatic bile ducts. Arch Pathol Lab Med 2010;134:e14-8.

27. Fiz F, Masci C, Costa G, Sollini M, Chiti A, Ieva F, Torzilli G, Viganò L. PET/CT-based radiomics of mass-forming intrahepatic cholangiocarcinoma improves prediction of pathology data and survival. Eur J Nucl Med Mol Imaging 2022;49:3387-400.

28. Peng YT, Zhou CY, Lin P, Wen DY, Wang XD, Zhong XZ, Pan DH, Que Q, Li X, Chen L, He Y, Yang H. Preoperative Ultrasound Radiomics Signatures for Noninvasive Evaluation of Biological Characteristics of Intrahepatic Cholangiocarcinoma. Acad Radiol 2020;27:785-97.

29. Lu W, Zhong L, Dong D, Fang M, Dai Q, Leng S, Zhang L, Sun W, Tian J, Zheng J, Jin Y. Radiomic analysis for preoperative prediction of cervical lymph node metastasis in patients with papillary thyroid carcinoma. Eur J Radiol 2019;118:231-8.

30. Huang YQ, Liang CH, He L, Tian J, Liang CS, Chen X, Ma ZL, Liu ZY. Development and Validation of a Radiomics Nomogram for Preoperative Prediction of Lymph Node Metastasis in Colorectal Cancer. J Clin Oncol 2016;34:2157-64.

31. Wilson R, Devaraj A. Radiomics of pulmonary nodules and lung cancer. Transl Lung Cancer Res 2017;6:86-91.

32. Zheng YM, Yuan MG, Zhou RQ, Hou F, Zhan JF, Liu ND, Hao DP, Dong C. A computed tomography-based radiomics signature for predicting expression of programmed death ligand 1 in head and neck squamous cell carcinoma. Eur Radiol 2022;32:5362-70.

33. Xu Q, Zhu Q, Liu H, Chang L, Duan S, Dou W, Li S, Ye J. Differentiating Benign from Malignant Renal Tumors Using T2- and Diffusion-Weighted Images: A Comparison of Deep Learning and Radiomics Models Versus Assessment from Radiologists. J Magn Reson Imaging 2022;55:1251-9.

34. Xiang F, Wei S, Liu X, Liang X, Yang L, Yan S. Radiomics Analysis of Contrast-Enhanced CT for the Preoperative Prediction of Microvascular Invasion in Mass-Forming Intrahepatic Cholangiocarcinoma. Front Oncol 2021;11:774117.

35. Addeo P, Jedidi I, Locicero A, Faitot F, Oncioiu C, Onea A, Bachellier P. Prognostic Impact of Tumor Multinodularity in Intrahepatic Cholangiocarcinoma. J Gastrointest Surg 2019;23:1801-9.

36. Atanasov G, Schierle K, Hau HM, Dietel C, Krenzien F, Brandl A, Wiltberger G, Englisch JP, Robson SC, Reutzel-Selke A, Pascher A, Jonas S, Pratschke J, Benzing C, Schmelzle M. Prognostic Significance of Tumor Necrosis in Hilar Cholangiocarcinoma. Ann Surg Oncol 2017;24:518-25.

References

37. Jin KP, Sheng RF, Yang C, Zeng MS. Combined arterial and delayed enhancement patterns of MRI assist in prognostic prediction for intrahepatic mass-forming cholangiocarcinoma (IMCC). Abdom Radiol (NY) 2022;47:640-50.

38. Liao X, Zhang D. The 8th Edition American Joint Committee on Cancer Staging for Hepato-pancreato-biliary Cancer: A Review and Update. Arch Pathol Lab Med. 2021;145(5):543-553.

39. Aherne EA, Pak LM, Goldman DA, Gonen M, Jarnagin WR, Simpson AL, Do RK. Intrahepatic cholangiocarcinoma: can imaging phenotypes predict survival and tumor genetics? Abdom Radiol (NY) 2018;43:2665-72.

40. Renzulli M, Brocchi S, Cucchetti A, Mazzotti F, Mosconi C, Sportoletti C, Brandi G, Pinna AD, Golfieri R. Can Current Preoperative Imaging Be Used to Detect Microvascular Invasion of Hepatocellular Carcinoma? Radiology 2016;279:432-42.

41. Mulé S, Galletto Pregliasco A, Tenenhaus A, Kharrat R, Amaddeo G, Baranes L, Laurent A, Regnault H, Sommacale D, Djabbari M, Pigneur F, Tacher V, Kobeiter H, Calderaro J, Luciani A. Multiphase Liver MRI for Identifying the Macrotrabecular-Massive Subtype of Hepatocellular Carcinoma. Radiology 2020;295:562-71.

42. King MJ, Hectors S, Lee KM, Omidele O, Babb JS, Schwartz M, Tabrizian P, Taouli B, Lewis S. Outcomes assessment in intrahepatic cholangiocarcinoma using qualitative and quantitative imaging features. Cancer Imaging 2020;20:43.

43. Sheng R, Huang X, Jin K, Gao S, Zeng M, Wu D, Shi G. Contrast-enhanced MRI could predict response of systemic therapy in advanced intrahepatic cholangiocarcinoma. Eur Radiol 2022;32:5156-65.

44. Lee J, Kim SH, Kang TW, Song KD, Choi D, Jang KT. Mass-forming Intrahepatic Cholangiocarcinoma: Diffusion-weighted Imaging as a Preoperative Prognostic Marker. Radiology 2016;281:119-28.

45. Min JH, Kim YK, Choi SY, Kang TW, Lee SJ, Kim JM, Ahn S, Cho H. Intrahepatic Mass-forming Cholangiocarcinoma: Arterial Enhancement Patterns at MRI and Prognosis. Radiology 2019;290:691-9.

46. Yoh T, Cauchy F, Le Roy B, Seo S, Taura K, Hobeika C, Dokmak S, Farges O, Gelli M, Sa Cunha A, Adam R, Uemoto S, Soubrane O. Prognostic value of lymphadenectomy for long-term outcomes in node-negative intrahepatic cholangiocarcinoma: A multicenter study. Surgery 2019;166:975-82.

Table S1 MR imaging acquisition protocols

Parameter	T1-weighted IP and OP imaging	T2-weighted images (coronal)	T2-weighted imaging FS	Diffusion-weighted imaging	CE T1- weighted imaging	Late post-contrast (coronal)
Repetition time (ms)	3.6-4.5	957-10000	1440-7000	1248-4000	2.9-3.8	3.6-5.4
Echo time (ms)	1.2-2.9	68-94	76-100	46-76	1.1-1.6	1.0-2.6
Field of view (cm)	36-42	38-42	36-38	36-38	36-42	40-50
Acquisition matrix	288×224, 256×224, 320×193	320×288, 288×288, 320×224	320×224, 320×320, 320×220	140×140, 128×128, 128×83	256×192, 288×224, 288×151	352×256, 288×256, 288×185
Pixels (mm)	0.6-1.0	0.6-1.2	0.9-1.3	1.4-1.9	0.3-0.5	0.5-1.7
Temporal resolution (s/phase)	NA	NA	NA	NA	12-16.6	15-33
Section thickness (mm)	3.0-6.0	5.0-7.0	5.0-6.5	6.0-7.0	3.0-5.0	1.5-4.2
Gap (mm)	0.5-1.0	1.0	0.5-1.0	1.0-2.0	0	0
Flip angle (degree)	9-15	90, 145	150, 120	90	9-15	9-15

Data is the range of parameters on different magnetic resonance image machines. Except specifically mentioned, they are all scanned on the axial. MR, magnetic resonance; IP, in-phase; OP, opposed-phase; FS, fat-suppressed; CE, contrast-enhanced; NA, not applicable.

Table S2 MR imaging features: definition of imaging features and respective categories

Variables	Definitions	Categories
Tumor maximum diameter (37)	Tumor maximum diameter was measured the largest diameter on axial pre-contrast T1-weighted image. Based on the 8th edition of the American Joint Committee on Cancer (AJCC) staging system, the tumors were divided into two groups (38)	1, ≤5 cm; 2, >5 cm
Number of tumors (39)	Number of tumors was determined based on the number of tumor nodules in the liver, including satellite nodules and intrahepatic metastasis. Satellite nodules defined as tumors within 1 cm of the primary tumor border, and intrahepatic metastases defined as tumors >1 cm from the primary tumor	1, single; 2, multiple
Tumor margin (40)	Smooth: a clear demarcation of the entire tumor on the MRI images obtained in the delayed phase or transitional phase. Non-smooth: focal extranodular extension, multinodular confluent appearance, and focal infiltrative margin in the delayed phase	1, smooth; 2, infiltrative
Tumor necrosis (41)	Necrosis sign was a continuously unenhanced defect with high-signal intensity on T2-weighted fat-suppressed image and low signal on T1-weighted image	1, absent; 2, present
Bile duct dilatation	Evaluated on T2-weighted fat-suppressed or contrast enhanced images, including inner-tumor or peritumoural bile duct dilation	1, absent; 2, present
Hepatic capsule retraction (42)	unequivocal inward liver contour changes immediately superficial to an intrahepatic cholangiocarcinoma lesion	1, absent; 2, present
Peritumoral enhancement (43)	Fuzzy-marginated hyperenhancement outside the tumor borders on arterial-phase (AP) that becomes isointense with normal liver parenchyma in later dynamic phases	1, absent; 2, present
DWI signal characteristics (44)	Diffuse hypo-enhancement: less than one-third of the tumor showed diffusion restriction. Diffuse hyper-enhancement: more than one-third of the tumor showed diffusion restriction	1, diffuse hypo-enhancement; 2, diffuse hyper-enhancement
AP enhancement pattern (45)	Diffuse hypo-enhancement: the area of hyperenhancement was less than 10% of the tumor surface. Rim-enhancement: rim-enhancement, the area range of peripheral enhancement was 10%–70%. Diffuse hyper-enhancement: the area of hyper-enhanced was greater than 70% of the tumor surface	1, Diffuse hypo-enhancement; 2, rim-enhancement; 3, diffuse hyper-enhancement
Targetoid appearance (43)	Targetoid appearance including one of the following: rim arterial phase hyperenhancement, peripheral washout, delayed central enhancement, or targetoid restriction on diffusion-weighted imaging	1, absent; 2, present
Lymph node status (46)	When a lymph node presented 1 cm at least in short-axis diameter or a smaller lymph node with heterogeneous enhancement, round or irregular shape was considered as positive	1, positive; 2, negative

MR, magnetic resonance; DWI, diffusion-weighted images.

Table S3 Inter-observer agreements for each imaging feature

Variables	κ values (95% confidence intervals)
Number of tumors	0.888 (0.815, 0.961)
Tumor margin	0.761 (0.679, 0.843)
Necrosis	0.749 (0.657, 0.841)
Bile duct dilatation	0.874 (0.807, 0.941)
Capsule retraction	0.831 (0.757, 0.904)
Peritumoral enhancement	0.872 (0.805, 0.939)
DWI signal characteristics	0.767 (0.649, 0.885)
AP enhancement pattern	0.792 (0.712, 0.872)
Targetoid appearance	0.634 (0.516, 0.752)
Lymph node status	0.863 (0.794, 0.932)

Data are κ statistics with 95% confidence intervals in parentheses.

Table S4 Radiomics features' selection results

|	Radiomic features	LASSO coefficient (β)
MVI status	Intercept	-0.09098416
	DWI_log.sigma.3.0.mm.3D_glrlm_LongRunLowGrayLevelEmphasis	0.22746793
	T2_log.sigma.5.0.mm.3D_glcm_ClusterShade	-0.08352660
	T2_log.sigma.2.0.mm.3D_glcm_Imc2	-0.01070164
	T2_wavelet.HHL_glszm_ZoneEntropy	0.14848064
	DWI_wavelet.HHH_glcm_SumEntropy	0.01244092
	T2_wavelet.LHH_firstorder_Kurtosis	0.08712179
	T2_wavelet.LLL_glszm_SmallAreaLowGrayLevelEmphasis	-0.16539808
	T2_log.sigma.5.0.mm.3D_firstorder_Skewness	-0.11850991
	DWI_original_shape_Flatness	-0.01091418
	T2_wavelet.HHL_gldm_DependenceVariance	0.12000406
	DWI_wavelet.HLL_glszm_SmallAreaHighGrayLevelEmphasis	0.14940092
	T2_wavelet.HHH_firstorder_Median	-0.09095953
	T2_wavelet.LHL_gldm_DependenceEntropy	0.03645931
	T2_wavelet.LLL_glcm_Imc2	-0.17710026
	DWI_wavelet.HHL_gldm_DependenceNonUniformityNormalized	-0.21121682
	T2_wavelet.LHH_glszm_ZoneEntropy	0.02886081
Tumor grading	Intercept	0.4957142100
	T2_wavelet.LHH_glcm_JointEnergy	-0.1130100795
	T2_wavelet.HLL_glcm_Imc1	0.0099504462
	DWI_wavelet.LLL_gldm_LargeDependenceHighGrayLevelEmphasis	0.0403740211
	T2_wavelet.LLH_glcm_Imc2	-0.0007046255
	T2_log.sigma.2.0.mm.3D_firstorder_Kurtosis	0.0731579396
	T2_wavelet.HLH_glcm_Imc1	0.1669030819
	DWI_log.sigma.2.0.mm.3D_glcm_Imc2	-0.0562923291
	DWI_original_shape_Elongation	0.2322154964
	T2_wavelet.HHH_gldm_DependenceVariance	-0.0848792990

The intraclass correlation coefficient of selected features all >0.8. MVI, microvascular invasion; DWI, diffusion-weighted images; LASSO, least absolute shrinkage and selection operator; glcm, gray-level co-occurrence matrix; glszm, gray-level size zone matrix; glrlm, gray-level run-length matrix; gldm, gray-level dependence matrix; log, Laplacian of Gaussian; H, high-pass filter; L, low-pass filter.

**Table S5** Comparison of different models by the Delong test

	Group	Model	Radiomics model	Nomogram model
MVI	Training set	Clinical model	0.326	<0.001
		Radiomics model	-	0.009
	Validation set	Clinical model	0.596	0.008
		Radiomics model	-	0.055
Tumor grading	Training set	Clinical model	0.003	<0.001
		Radiomics model	-	0.313
	Validation set	Clinical model	0.544	0.002
		Radiomics model	-	0.095

P values <0.05 was defined as statistical significance. MVI, microvascular invasion.
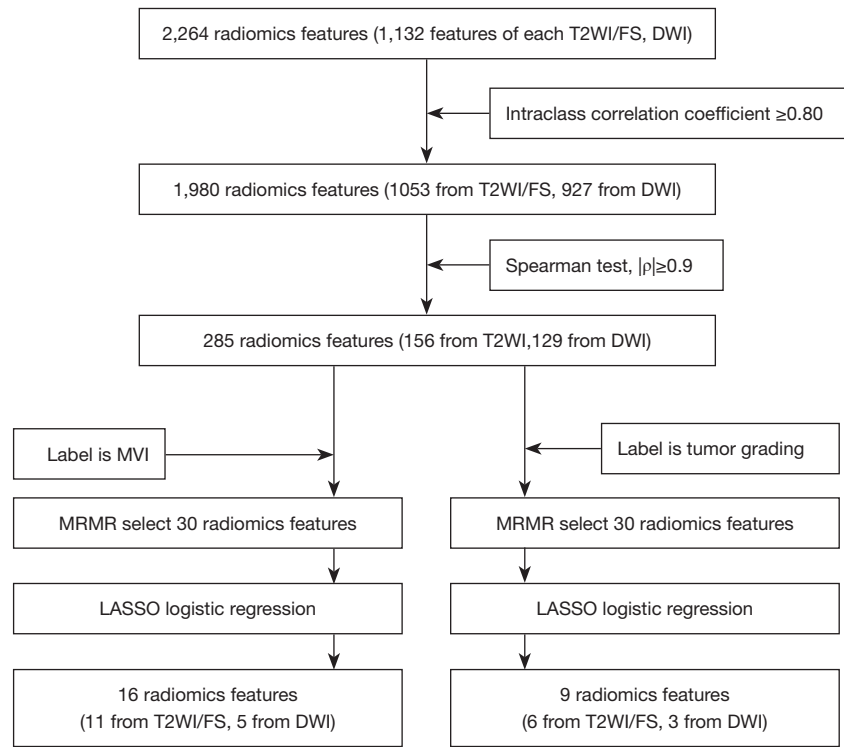
Figure S1 Radiomics features selection pipeline. T2WI/FS, T2 weighted imaging/fat-suppressed; DWI, diffusion weighted imaging; MVI, microvascular invasion; MRMR, minimum redundancy maximum relevance; LASSO, least absolute shrinkage and selection operator.
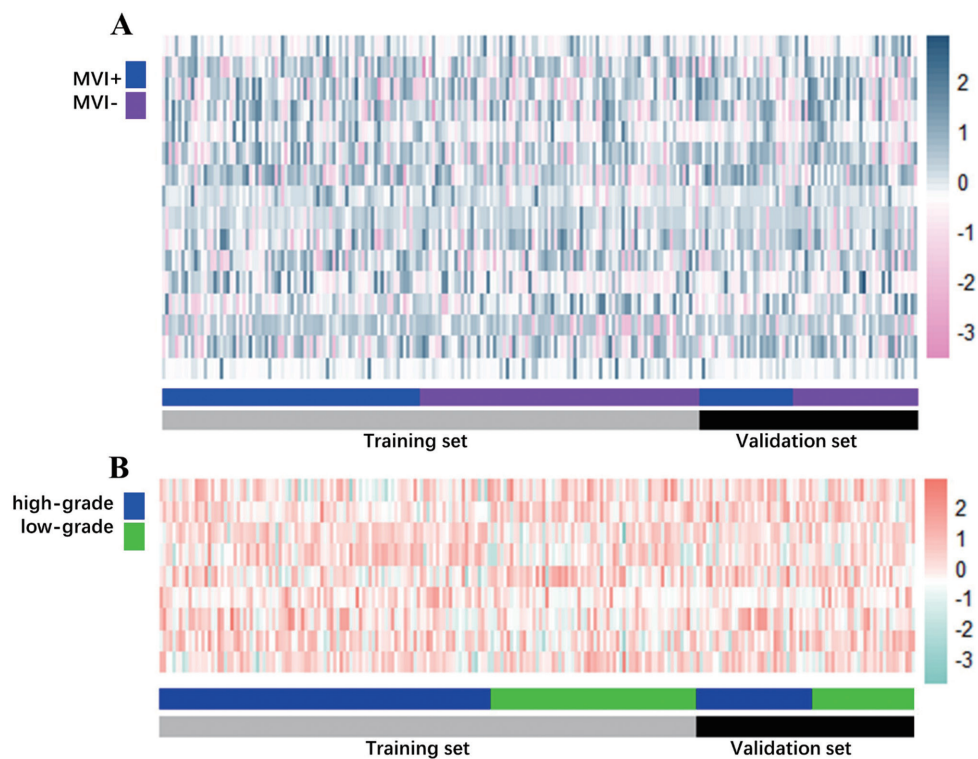

Figure S2 Heatmap of the significant radiomics features. Each column corresponds to one patient, and each row corresponds to the Z-scores of the normalized radiomics features. The heatmap is grouped for the training and validation sets for prediction of MVI (A) and tumor grading (B). Sixteen radiomics features were selected for MVI and 9 radiomics features were selected for tumor grading. MVI, microvascular invasion.
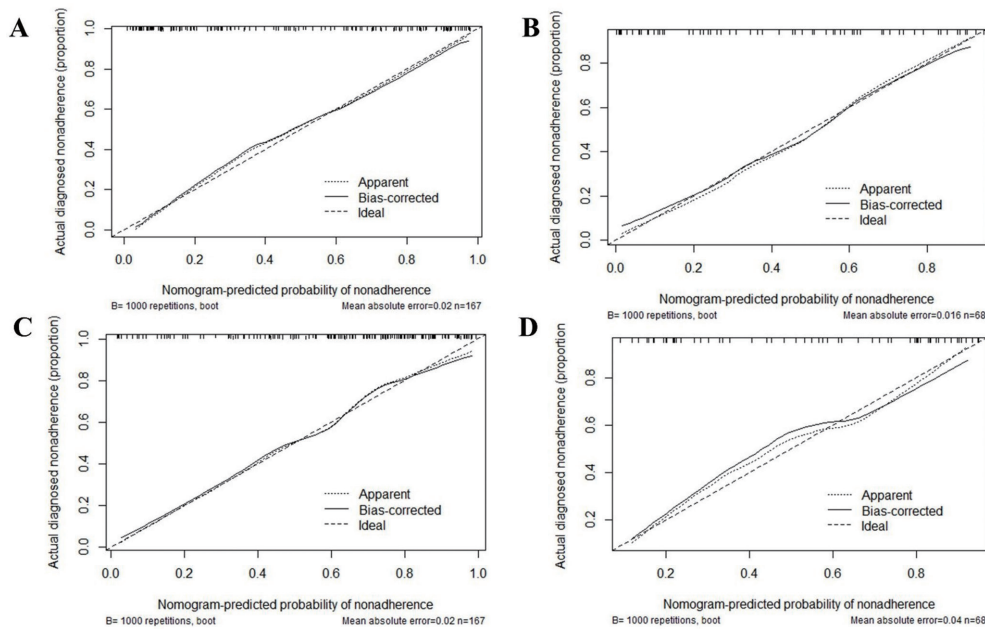
Figure S3 Calibration curve of the nomogram in training set for the prediction of MVI (A) and tumor high-grading (C). Calibration curve of the nomogram in validation set for the prediction of MVI (B) and tumor high-grading (D). The 45° dotted line represents a perfect prediction. The solid line represents the predictive performance of the nomogram. The solid line has a close fit to the dotted gray line, which indicates good predictive capability of the nomogram. Hosmer-Lemeshow test showed good calibration in the training (P=0.895) (A) and validation (P=0.762) (B) sets in the prediction of MVI. P values were 0.451 (C) and 0.254 (D) based on the Hosmer-Lemeshow test in the training and validation sets in the prediction of tumor grading. MVI, microvascular invasion.
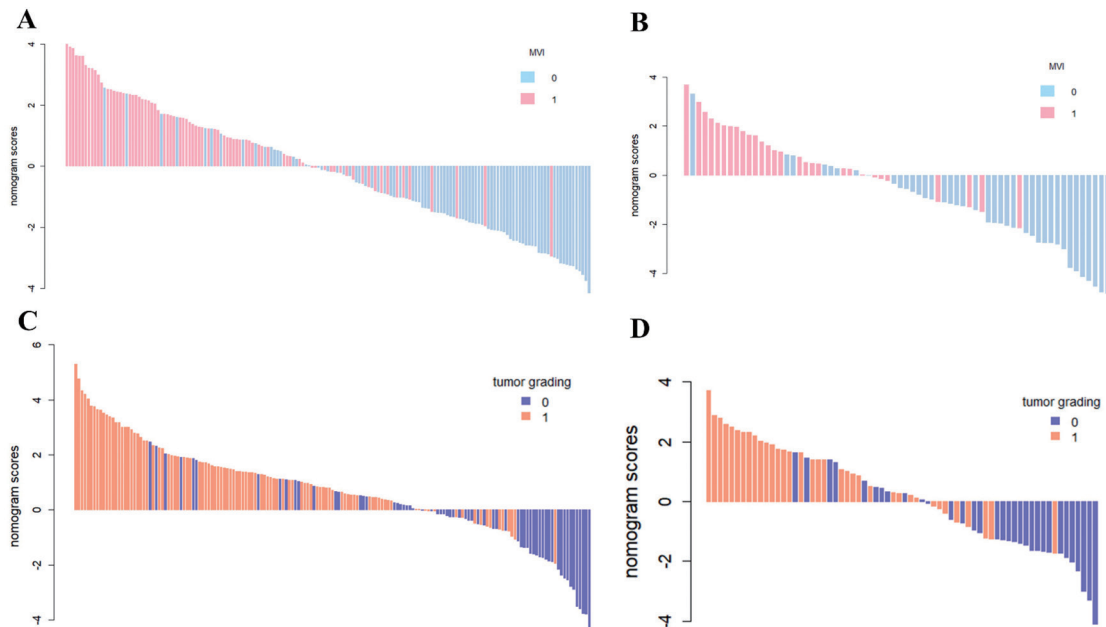
Figure S4 The radiomic nomogram scores for each patient in the training (A) and validation (B) sets for the prediction of MVI. The radiomic nomogram scores for each patient in the training (C) and validation (B) sets for the prediction of tumor grading. MVI, microvascular invasion.
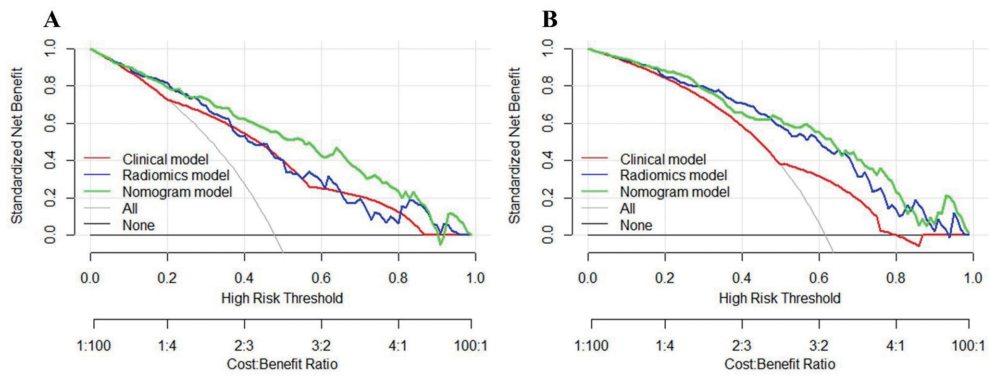
Figure S5 DCA for the radiomics nomogram in the training set. The x-axis represents the threshold probability, and the y-axis represents the net benefit. The "All" line represents the hypothesis that all patients had MVI (A) or high-grading (B). The "None" line indicates the hypothesis that no patients were MVI (A) or high-grading (B). The red (using clinical characteristics), blue (using radiomics signature), and green (using nomogram) lines represent the net benefits of different diagnostic models at given threshold probability for the prediction of MVI+ (A) and high-grading (B). DCA, decision curve analysis; MVI, microvascular invasion.